

## **TWO EXAMPLES OF ADDING VALUE THROUGH DIGITAL ROCK TECHNOLOGY**

J. Schembre-McCabe, R. Salazar-Tio, and J. Kamath

*Chevron Energy Technology Company, San Ramon, USA*

*This paper was prepared for presentation at the International Symposium of the Society of Core Analysts held in Aberdeen, Scotland, UK, 27-30 August 2012*

### **ABSTRACT**

Digital Rock Technology has experienced tremendous progress in the last decade with an increasing number of companies providing imaging hardware and software as well as delivering computational services. This technology is also commonly referred to as a transformational technology in different fronts and yet, because focus has been heavily placed in validating the technology, there are limited publications demonstrating its business value besides replacing experimental data. We have learned that validation, especially the deterministic approach, wanes the exploration of further use of this technology, and hence, we shifted our original mission of validation towards value demonstration. In this paper, we give our initial report after looking at potential uses of this technology.

We provide examples in which we use this technology to understand and reduce uncertainty in existing experimental data using an uncertainty-based framework that acknowledges the uncertainty in both computation and measurements. The workflow enables capturing the source of uncertainty in the experimental data, improves screening, understanding and interpretation of the experimental data. Another example highlights the use of the imaging technology in resolving drilling & completion issues in unconsolidated sands, where the distributions of effective pore diameters overcome limitations imposed by Mercury Injection data.

The digital rock world is coming, but its form and how it will emerge is still unclear. Hopefully, these two examples provide a foretaste among the many potential uses of this technology in a fast approaching future.

### **INTRODUCTION**

The capability of describing the pore space at the minimum contributing scale to flow, as well as the computing capacity to model processes through these structures looks promising to understand different phenomena in each of the sciences connected by these systems. We present two examples that explore applications of this technology to existent

experimental data to improve our understanding and surpass the challenges imposed by the limitations in experimental or interpretation techniques currently available.

## **IMPROVING UNDERSTANDING AND INTERPRETATION OF EXPERIMENTAL DATA**

One of the challenges during the analysis of experimental data is to separate effects of rock properties from the consequences brought by choice of experimental setup (process uncertainty) as well as experimental artifacts. In some instances, it is common to obtain wide range of results for samples with similar properties. The value of network models resides in their ability to relate macroscopic behavior directly to the underlying physics[1]. We describe the use of pore network modeling in understanding and identifying outliers in drainage and imbibition data for gas (CO<sub>2</sub>) storage; in this type of projects injectivity and residual gas are chief concerns.

To understand experimental data, we focus on samples that despite having similar properties (i.e. available pore space to flow and connectivity) exhibit differences in the flow properties, which lead to a wide range of injectivity and residual trapped saturations. For this specific case, we concentrate in experimental data corresponding to cores with properties ranges corresponding to FZI (Flow Zone Indicator) larger than 1.50; similarly we selected two samples from same zones and FZI ranges for simulation. The workflow to compute values from 3-D micro CT – images using experimental design is described elsewhere [2]. In this work, we concentrate in the results from images and their use in the analysis of experimental data.

### **Image Analysis**

The selection of an optimum resolution for the image is guided by the information supplied by Back-scatter SEM and QEMSCAN images; layers of clay coating of 4-6 microns were appreciated with 2-3 pixels in QEMSCAN 2D images in Figure 1 (resolution is 2 micron/pixel), hence images with resolution of 2.0 microns/pixel or smaller are recommended. For this analysis, we used micro-CT 3D images using a synchrotron source (LBNL<sup>1</sup>) with 1.8 microns/pixel resolution. This range of resolution is enough to capture main percolation paths for porosity and compute transport properties. Also, dimension of simulation volumes were almost as twice the minimum linear size required (2-3 mm) to be considered statistically representative volume as estimated from the decay curve in the porosity variogram. Because of the amount of clay and their distribution, the segmentation of these images is not trivial. Figure 2 shows the segmented back-scatter SEM images for sample 1 (left) and 2 (right).

---

<sup>1</sup> Advanced Light Source (ALS), third generation synchrotron at Lawrence Berkeley National Laboratory, Berkeley, California.

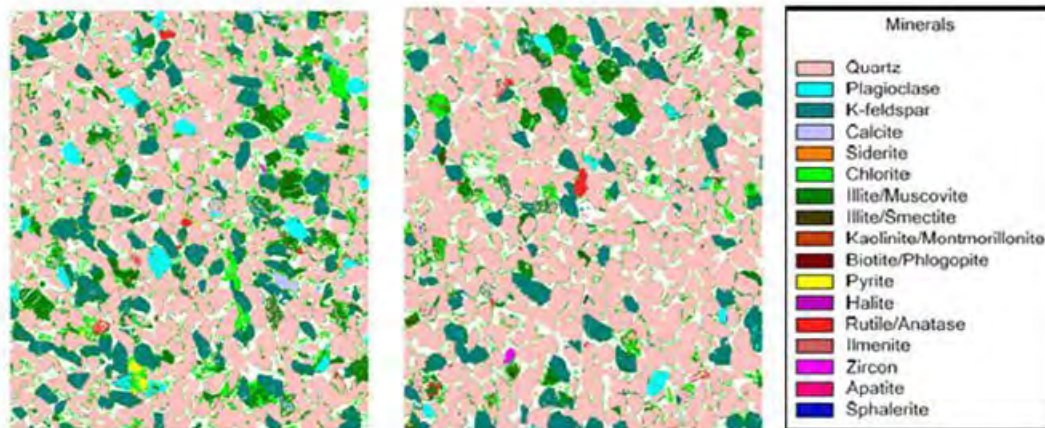


Figure 1: QEMSCAN image (resolution 2µm/pixel)

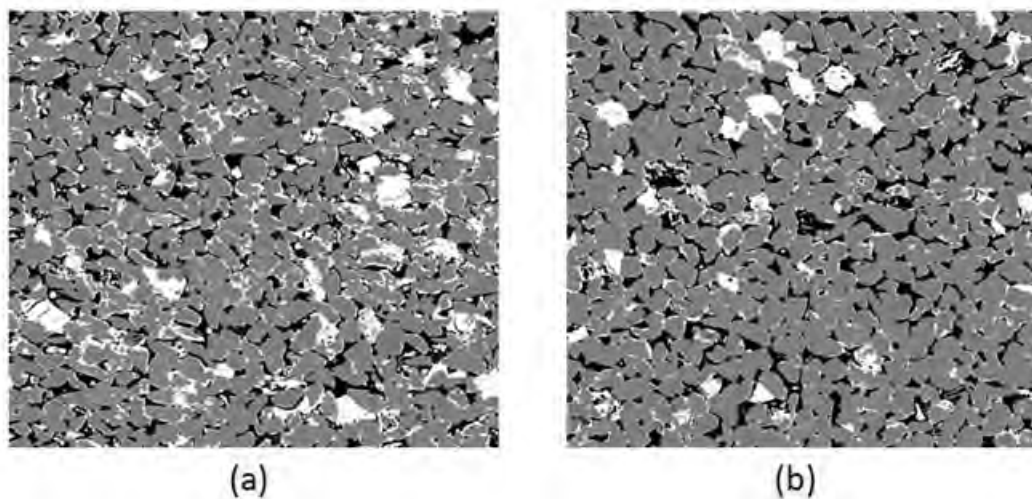


Figure 2: Back-scatter SEM images after segmentation for (a) Sample 1 (Pore 17.5%, Clay: 19.8%) and sample 2 (pore 17.4% and clay 13.6%)

This information provided by SEM, together with the QEMSCAN®, is used to narrow the uncertainty in the segmentation process, especially in samples with large amount of clay and sub-resolution pores. This increase in confidence in the phase identification is also discussed by Knackstedt *et al.*[3]. Figure 3 shows an example (sample 1) of a slide of 3D micro CT before (left) and after (right) segmentation. To narrow the uncertainty in the segmentation process we integrate total porosity values ( $\phi_{\text{total}}$ ) from neighboring samples with information such as intergranular porosity ( $\phi_{\text{pore}}$ ) and clay volume ( $V_{\mu}$ ) supplied by QEMSCAN® images and segmented back-scatter SEM images (Figure 2). The combined analysis provides a range of best estimate for clay phase

microporosity, ( $\overline{\phi}_{\mu}$ ). In this case, we obtained computed micro-porosity between 50 and 75% for sample 1 and between 57% and 90% for sample 2.

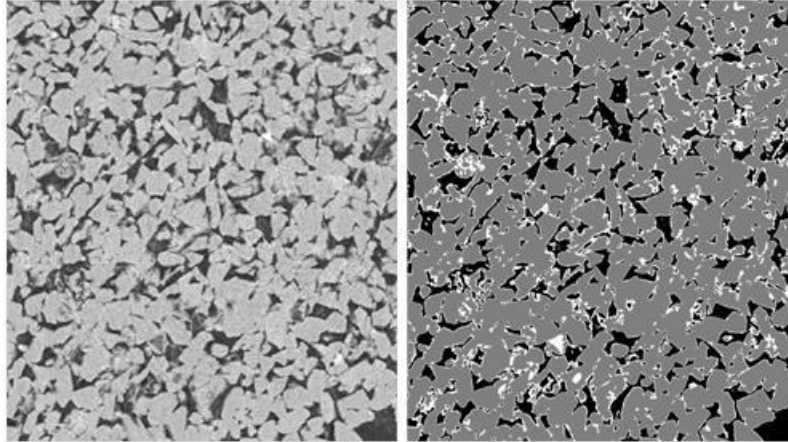


Figure 3: Example of segmentation process. Sample 1(left) Micro-CT and (right) segmented image

As a next step, we verify whether the pore network model<sup>2</sup>, extracted from segmented images, captures the rock structure features by comparing experimental and numerical data. Figure 4 compares J-functions corresponding to experimental measurements (Mercury Intrusion - black solid line) and computed using the pore network model. Same figure also showed experimental measurements in samples corresponding to target Flow Zone Indicator range ( $FZI \geq 1.5$ ). In both cases, estimated curves show good agreement with the experimental data. The agreement of results with experimental data indicates that the segmented images are capturing main features contributing to the flow in these samples.

---

<sup>2</sup> E-Core, Numerical Rocks. Version 1.5.2 (2012).

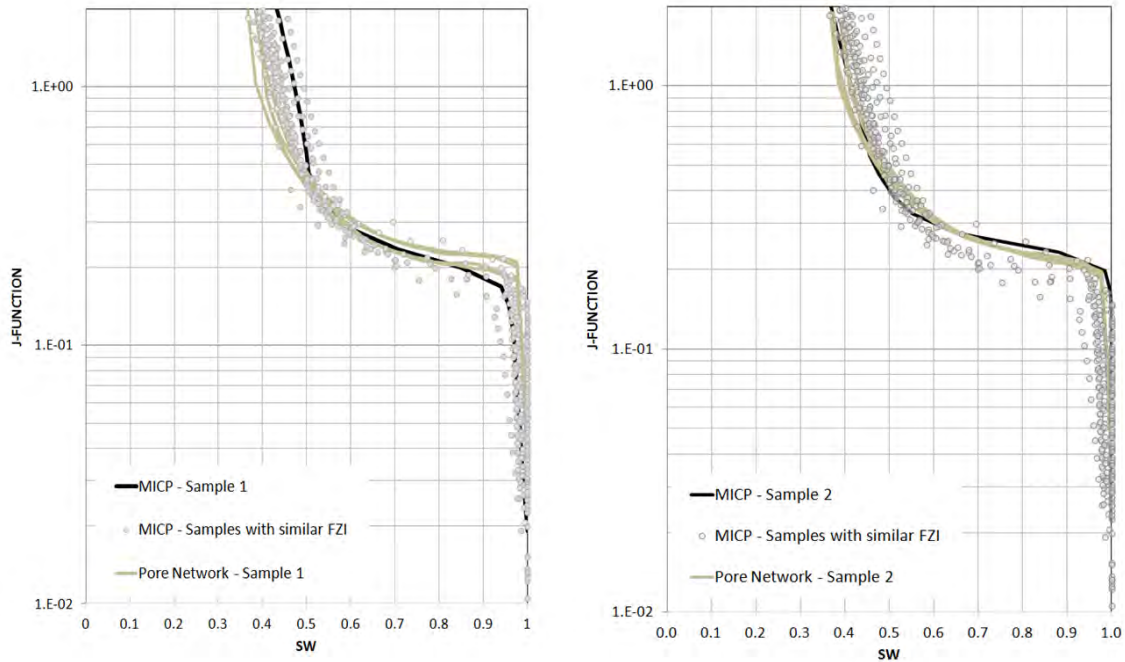


Figure 4: Experimental and Numerical Drainage J-function for Sample 1 (right) and 2 (left)

### Injectivity and Drainage Relative Permeability

Our recommendation in any SCAL program [4] is a 50-50 resource split between tests to capture geological variability (conducting simple tests on many samples) and process uncertainty (conducting specific tests on a sub-set of samples). In order to capture injectivity parameters, we measured drainage relative permeability performing standard gas-brine unsteady-state to capture effect of rock variability while process uncertainty was gauged by varying rates, changing type of tests and displacing fluids (nitrogen, decane, and CO<sub>2</sub>).

During the design of these tests, we should be targeting injection rates and pressure difference such that experimental capillary numbers match those reached during field operations. On the other hand, because capillary effects can significantly influence measurements especially low-rate drainage displacement [5], injection rates for these tests are typically high. An example of applying a range of rates to satisfy both conditions is shown in Figure 5; Steady state tests were performed at high rates for both (N<sub>2</sub>/Brine and CO<sub>2</sub>/Brine) systems, two Unsteady states were performed at low capillary number and endpoint tests were performed at ranges between both requirements. Table 1 shows details and capillary number reached during the experiments

Because all these tests are reported for samples with similar rock properties, the wide range of curves and endpoints,  $S_{wir}$  and  $(K_{rg}(S_{wir}))$  are, consequently, results of fluids and methodology used, target injection rates and/or experimental artifacts [6,7]. While the Brine relative permeability exhibited different mobility for different fluid system, the

largest uncertainty is towards the low water saturation range. Unsteady state test, performed a low capillary number and hence likely to be dominated by heterogeneities, experimental artifacts or limitations imposed by maximum capillary pressure, exhibit high residual water saturation and low gas relative permeability endpoints. Figure 5 also shows values estimated using pore network modeling in images of samples 1 and 2; The simulation data, not subject to experimental limitations previously mentioned, shows higher gas saturations and endpoints than values reached in endpoint experiments, which are suspected to be dominated by either capillary end effects or artifacts.

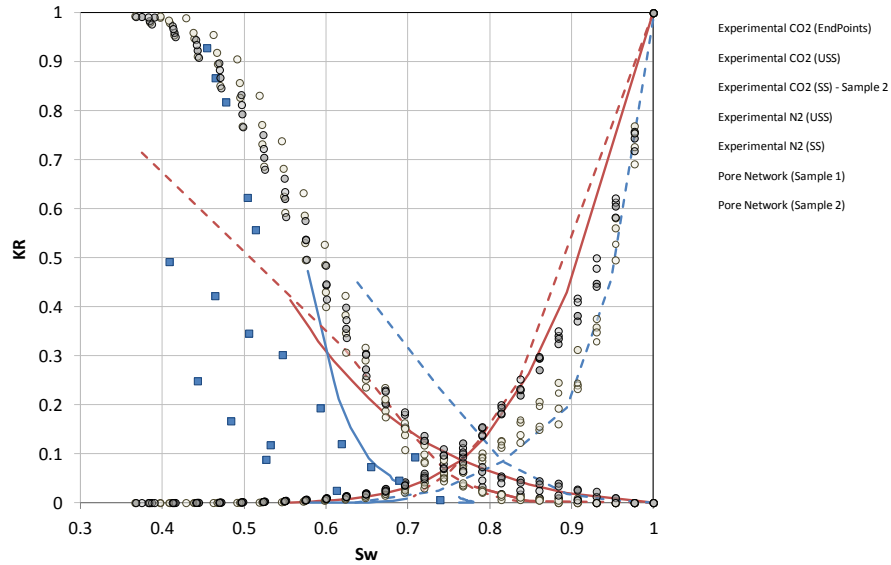


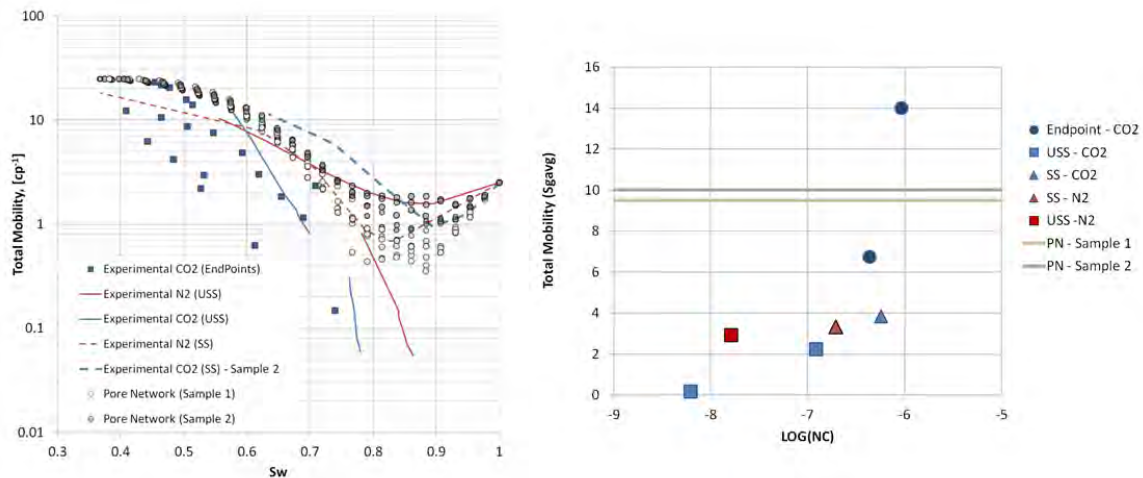
Figure 5: Experimental and Numerical Drainage relative permeability (legend in Table 1)

Table 1: Details of drainage relative permeability shown in Fig. 6

Sample	System	Method	Log [Nc]	Symbol
1	CO <sub>2</sub> /Brine	Coreflood Endpoint	Between -7.2 and -5.6	■
2	CO <sub>2</sub> /Brine	Coreflood Endpoint	Between -8.0 and -7.3	
3	CO <sub>2</sub> /Brine	Coreflood Endpoint	Between -6.2 and -5.9	
4	CO <sub>2</sub> /Brine	Coreflood Endpoint	Between -8.2 and -5.9	
5	CO <sub>2</sub> /Brine	Coreflood Endpoint	Between -8.2 and -5.9	
2	CO <sub>2</sub> /Brine	Unsteady State	-8.2	—
3	CO <sub>2</sub> /Brine	Unsteady State	-6.9	—
6	N <sub>2</sub> /Brine	Unsteady State	-7.8	—
7	CO <sub>2</sub> /Brine	Steady State ( $f_g=1$ )	-6.2	- - -
8	N <sub>2</sub> /Brine	Steady State ( $f_g=1$ )	-6.7	- - -
Image 1	Numerical Modeling			●
Image 2	Numerical Modeling			●

To better understand the impact of these ranges on injectivity, we borrow the concept of total mobility. Injectivity depends strongly on the mobility of the two-phase flow region

([8, 9]) and total mobility plots are very useful when comparing different sets of relative permeability, especially the average mobility in the Buckley-Leverett region [9]. The left plot in Figure 6 shows the corresponding total mobility using viscosities at field conditions while the right chart compares the total mobility evaluated at average saturation in the Buckley-Leverett region vs. experimental capillary number; this plot illustrates the cascading effect of the uncertainty in relative permeability parameters in injectivity and it warrants much closer inspection of the experimental data.



**Figure 6: Total Mobility plot computed used field viscosity (left) and Total Mobility evaluated at average saturation in the Buckley-Leverett region vs. Capillary number reached during experiment**

A closer inspection of the experimental data requires numerical modeling of the experiments. Relative permeability estimated from pore network provides us with a potential best estimate for multiple variable regression input in the history match of experiments, especially when we suspect that experiment did not reach the minimum water saturation. Multivariable analysis is used for the parameters used in the LET function [10] defining relative permeability in the history matching of pressure and production history during coreflood. Figure 7 shows the raw experimental data (black) from CO<sub>2</sub>/Brine Steady State test, symbols are drainage relative permeability estimated from pore network simulation on sample 2 (which is a sub-sample of the core used in this experiment). The red lines represent the final relative permeability after using the pore network relative permeability as the first guess in the Parameter Estimation<sup>3</sup>. The experimental and final Steady State data are in close agreement, and the final curve extends the gas relative permeability to lower water saturations and higher gas relative permeability endpoints.

<sup>3</sup> Sendra Version 1.10, User Guide, Reslab Integration AS, Nov 2007

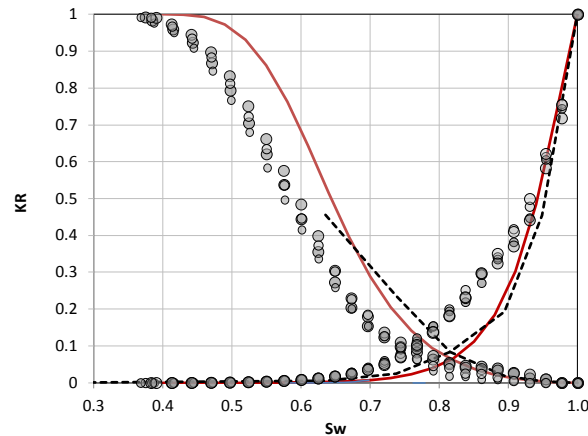


Figure 7: Raw experimental data (black dashed line) and output (red) drainage relative permeability after using multiple variable regression to match experimental CO<sub>2</sub>/Brine coreflood at reservoir conditions

### **Residual Gas Saturation**

In the case of residual gas, we use Countercurrent Imbibition (CCI) to gauge geological variability while process uncertainty is captured by performing Unsteady- and Steady-state imbibition with different displaced fluids. Figure 8 shows that trapped (residual) non-wetting phase values from pore network simulations are in agreement with the range of values shown in experimental data, especially with the values obtained from Countercurrent imbibition tests (CCI). This is expected because both CCI and numerical simulation are in the low capillary number regime in which capillary forces are dominant. In the case of residual CO<sub>2</sub>, we did not have experimental values available in these sands to compare numerical results. It is our expectation that comparison of numerical results with experimental results could provide an opportunity to understand and calibrate calculations for the effects of higher capillary numbers and wettability of Brine/CO<sub>2</sub> systems in experimental measurements as well as the identification of outliers.

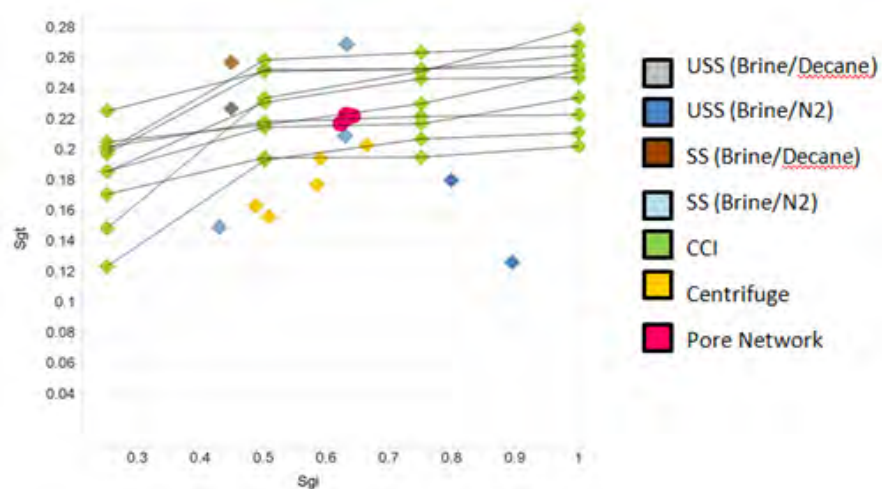


Figure 8: Experimental and Numerical Trapped Residual Non-wetting saturation

## DRILLING AND COMPLETION IN UNCONSOLIDATED SANDS

Formation rock attributes are considered as a key factor in optimizing reservoir drilling fluids with capabilities to limit fluid losses and minimize solid plugging effectively. For the purposes of determining the sizes of bridging material, Mercury Intrusion capillary pressure (MICP) provides information on the diameter of the largest connected pore space. However, the major disadvantage of using MICP is that it may not detect the largest pores in some reservoir formations; for this specific example, onset Hg injection pressures resulted in truncation of the pore throat radius at 100 microns which excluded larger pore throats that fill up at lower injection pressures (approximately 0.4 to 1 psi).

Other methods that are commonly used to characterize pore structure are Scanning Electron Microscopy (SEM) and thin-section analysis; SEM focus in very small fraction of the rock and, hence, it is not practical for finding the largest pores and thin sections have the disadvantage that it offers only a 2D view of a 3D structure[11]. In addition, increased pore space could be artificially created due to the separation of grains during preparation of 2D section while polishing unconsolidated rocks. We used to x-ray CT 3D images of cores plugs (1.5 inch in diameter) to estimate the pore size distribution of large pores. With a resolution of 28  $\mu\text{m}/\text{pixel}$  we have the advantage of covering a larger volume, thus benefiting the statistics of the larger pores within the sample. We pre-filtered the 3D image by applying a Gaussian filter of sigma value of 2 pixels, which will tend to smooth out small features such as small pores, small pore throats, and some pore irregularities. Then, single threshold is applied to the image to highlight the larger pores. Figure 10 shows one out of a set of 2000 slices detailing pore contours in yellow.

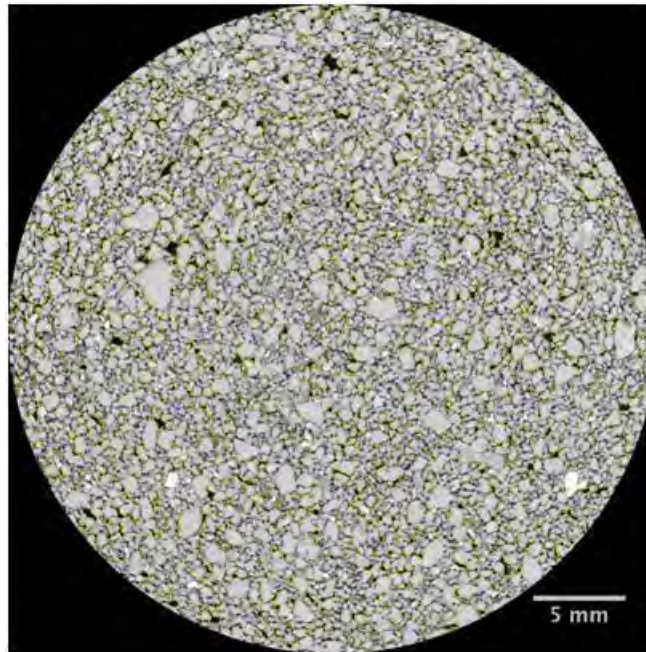


Figure 9: Micro-CT image of sample with cementation issues

We used two methods to estimate the size distribution of these large pores;

1. Local thickness based method: this method estimate the local thickness at each point together with the diameter of the greatest sphere fitting within the pore structure contains the reference point. This is a two step process and involves the computation of the Euclidean distance map followed by Maximal Inscribed Sphere map [12]. A histogram from values in the second step gives us a pore size distribution.
2. The second method estimates the Feret's diameter of individual pores; Feret's diameter is defined as the longest distance between two points along the pore boundary [13].

Figure 10 compares pore size distribution applying both methods. In both methods, especially in the Feret's diameter analysis, it is necessary to include pre-filter Gaussian step to highlight and separate larger pores. For this analysis, we observed pores larger than 200-300 microns diameter. Absence of this information would result in selecting bridging particles sizes too small to adequately protect the formation; as a result, this information proved to be extremely useful during selection of the right drilling fluid formulation.

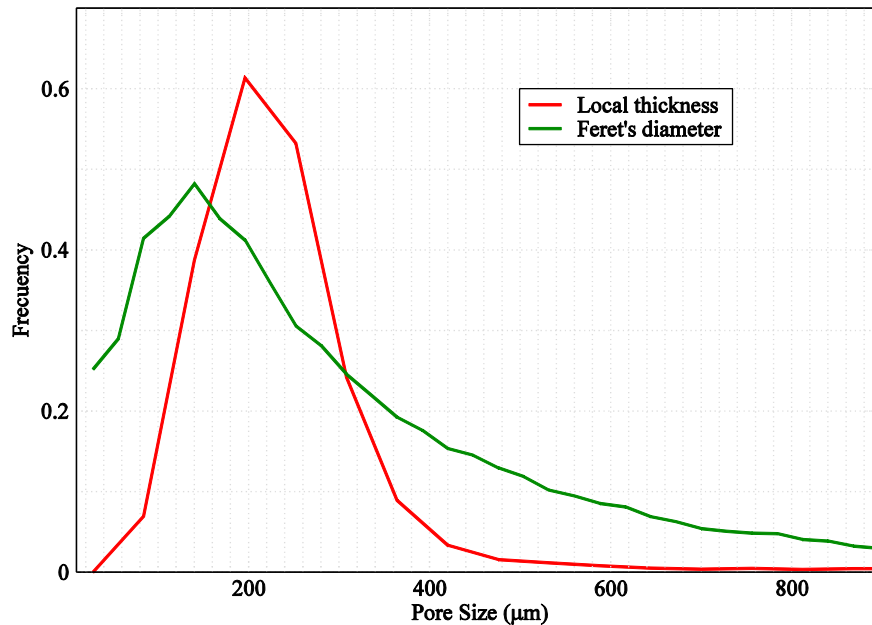


Figure 10: Local thickness and Feret's diameter distributions for the estimation of large pore sizes in sample shown in figure 10.

## CONCLUSIONS

- The segmentation process of images benefits from using additional information, especially for samples with large amount of clay and sub-resolution features such as these samples.
- Results from simulation on pore network model could be used to identify rate effects and experimental artifacts suspected in experimental data, assisting the reduction of the uncertainty in the properties measured and metrics affected by these properties.
- Micro-CT images provide useful information to assist with proper selection of drilling fluids, especially in cases where MICP data is not able to provide the information on the larger pore throats that fill at very low injection pressures.

## ACKNOWLEDGMENTS

Authors acknowledge Chevron management and Chevron Asia Pacific Exploration & Production Company for their support and permission to publish these results. We thank Maricel Marquez, Julie Cass, Scott Anderson and Jeroen Brantjes for their contribution in the discussion of application of this technology in drilling and completion operations.

## REFERENCES

1. Øren, P.E. and S. Bakke, "Reconstruction of Berea Sandstone and pore-scale modeling of wettability effects," *Journal of Petroleum Science and Engineering* (2003), 39, 177-199.

2. Schembre-McCabe, J., Salazar-Tio, R., Ball, G., and J. Kamath, "A framework to validate Digital Rock Technology," *Proceedings of the 2011 International Symposium of the Society of Core Analysts*, Austin (2011), SCA 2011-028.
3. Knackstedt, M., J. Patricio, A.R. Burcher, P.Botha, J. Middleton, and R. Sok, "Integrating Reservoir Characterization: 3D Dynamic, Petrophysical and Geological Description of Reservoir Facies," proceedings of the SPE Asia Pacific Oil & Gas Conference and Exhibition, (2010), SPE 133981.
4. Kamath, J., F. Nakagawa, J. Schembre, T. Fate, E. deZabala, P. Ayyalasomayajula, "Core Based Perspective on Uncertainty in Relative Permeability," *Proceedings of the International Symposium of the Society of Core Analysts*, Toronto (2005), SCA 2005-30.
5. Sigmund, P.M. and F. G. McCaffery, "An Improved Unsteady-State Procedure for Determining the Relative-Permeability Characteristics of Heterogeneous Porous Media," *Proceedings of the SPE Annual Technical Conference and Exhibition*, Denver (1977), SPE 6720
6. LeFebvre Du Prey, E. J., "Factors affecting Liquid-Liquid Relative Permeabilities of a Consolidated Porous Medium," *Journal of Petroleum Technology* (1973), February, 39-47.
7. Fulcher Jr. R. A., Ertekin, T. and C. D Stahl, "Effect of Capillary Number and its constituents on Two-Phase Relative Permeability Curves," *Journal of Petroleum Technology* (1985), February, 249-260.
8. Schembre-McCabe, J., Kamath, J. and R. Gurton, "Mechanistic Studies of CO<sub>2</sub> Sequestration," *Proceedings of the International Petroleum Technology Conference*, Dubai (2007), DOI: 10.2118/11391-MS
9. Burton M., Kumar, N. and S. Bryant, "Time-dependent Injectivity during CO<sub>2</sub> Storage in Aquifers," *Proceedings of the 2008 SPE/DOE Improved Oil Recovery Symposium*, Tulsa (2008). DOI: 10.2118/113937-MS
10. Lomeland, F., Ebeltoft, E. and T. W. Hammervold. "A New versatile Relative Permeability Correlation," *Proceedings of the international Symposium of the Society of Core Analysts*, Toronto (2005), SCA2005-32
11. He, W. and Stephens, M.. "Bridging Particle Size Distribution in Drilling Fluids and Formation Damage," *Proceedings of the 2011 SPE European Formation Damage Conference*, Noordwijk (2011). SPE 143497.
12. Silin, D, B. and T. W. Patzek, "Robust determination of the pore space morphology in sedimentary rocks," *Soc. Petrol. Eng. J.* (2003), 8429
13. Nature, Volume 162, Issue 4113, pp. 329-330 (1948).